Experimental Analysis of Dynamic Interactions between Micrometer-Scale Stainless Steel Spheres

Thesis by: Gladia Hotan

Mentor: Professor Chiara Daraio

Co-Mentor: Wei-Hsun Lin

In Partial Fulfillment of the Requirements for the degree of

Bachelor of Science in Physics

CALIFORNIA INSTITUTE OF TECHNOLOGY

Pasadena, California

[2013]

Acknowledgements

I would like to thank Professor Daraio for giving me the opportunity to work in her laboratory, and my co-mentor, Wei-Hsun, for his patient tutelage and for being there to guide me every step of the way.

Table of Contents

Abstract

The quasi-static interactions between macroscopic, spherical particles are well described by the Hertzian contact law. However, little is known about the interaction law at the micrometer scale, where the effects of electrostatic and hydrodynamic forces at the contact are no longer negligible. Contact dynamics at the micrometer scale have been relatively unexplored due to experimental challenges, since the particles are too small in size to be excited by actuators but too massive to be manipulated by electromagnetic fields. In this work, we experimentally study the dynamic interactions between two micrometer-scale spheres colliding in a v-shaped groove. From our experiments we determine physical parameters of interest that inform us about the force laws that apply before, during and after the collision. These parameters include the coefficient of air resistance, the coefficient of friction between the spheres and the groove, the coefficient of friction between two spheres in contact, and the coefficient of restitution.

Motivations for Work

A fundamental understanding of the laws controlling the dynamic interactions between micrometer-scale particles is relevant to many applied areas, ranging from the large-scale fabrication of microelectronic devices (where, for example, the interaction of wafers with dust particles represents one of the biggest fabrication challenges) to the flow and packing of granular particles in pharmaceutical and chemical applications.

In particular, metamaterials research involves the creation of new materials from periodically arranged repeated subunits. The arrangement of the subunits is engineered such that the metamaterial exhibits novel desired material properties. Extensive research in the Daraio lab has been carried out on soliton wave propagation in 1D, 2D and 3D periodic arrangements of centimeter-scale stainless steel spheres. An understanding of the contact dynamics for micrometer-scale stainless steel spheres will pave the way for the creation of new metamaterials that exploit the unique properties of these smaller spheres.

1. Literature Review

1.1 The Hertzian contact force between spheres

1.2 Molecular adhesion between spheres: The Derjaguin-Muller-Toporov model

1.3 Dissipative forces

- 1.3.1 Dissipation during sliding motion
- 1.3.2 Dissipation during rotational motion

1.4 The coefficient of restitution

1.1 The Hertzian contact force between spheres

The interactions between spherical particles initially in point contact are governed by the quasistatic Hertzian force[1], $F_{Hertz} = K\mathrm{h}^{3/2}$, where $K = \frac{E\sqrt{2R}}{3(1-\sigma^2)}$, R is the radius of the spheres, E is the elastic Young's modulus, σ is the Poisson ratio and h is the deformation of the spheres, which is given by the separation between the centers of adjacent spheres minus the sum of their radii.

The Hertzian force is derived by considering the pressure between the two deformed spheres inside the region of contact C. In general C is an ellipse with axes a and b. By substituting $u_z = \frac{1-\sigma^2}{\pi E} \iint_C \frac{P_z(x,y)}{r} dxdy$ into the equation describing the geometry, $Ax^2 + By^2 + u_z + u_z' = h$, we obtain the equation to be solved for the pressure distribution in the region of contact:

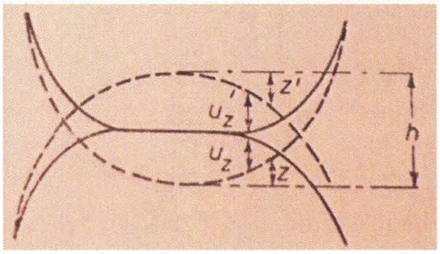

Fig 1.1a. Figure from ref [2] showing geometry being discussed.

$$\frac{1}{\pi}\left(\frac{1-\sigma^2}{E} + \frac{1-\sigma'^2}{E'}\right) \iint_C \frac{P_z(x,y)}{r} dxdy = h - Ax^2 - By^2 \qquad \text{--- equation (1)}$$

Since this equation is equivalent to the equation for the potential inside a uniformly charged ellipsoid, the results from potential theory can be used to show that the pressure inside the region of contact is given by $P_z(x,y) \propto \sqrt{1 - \frac{x^2}{a^2} - \frac{y^2}{b^2}}$. By considering the relation between force and pressure, $F = \iint_C P_z(x,y)\, dxdy$, we obtain the exact expression for the pressure,

$$P_z(x,y) = \frac{3F}{2\pi ab}\sqrt{1 - \frac{x^2}{a^2} - \frac{y^2}{b^2}} \qquad \text{--- equation (2)}$$

Substitution of equation (2) into equation (1) gives elliptic integrals for h, A and B:

$$h = \frac{FD}{\pi}\int_0^\infty \frac{d\varepsilon}{\sqrt{(a^2+\varepsilon)(b^2+\varepsilon)\varepsilon}} \qquad \text{--- equation (3.1)}$$

$$A = \frac{FD}{\pi}\int_0^\infty \frac{d\varepsilon}{(a^2+\varepsilon)\sqrt{(a^2+\varepsilon)(b^2+\varepsilon)\varepsilon}} \qquad \text{--- equation (3.2)}$$

$$B = \frac{FD}{\pi}\int_0^\infty \frac{d\varepsilon}{(b^2+\varepsilon)\sqrt{(a^2+\varepsilon)(b^2+\varepsilon)\varepsilon}} \qquad \text{--- equation (3.3)}$$

In the case of two deformed spheres with equal radii, $= B = \frac{1}{R}$. Also, the region of contact is a circle, so set $a = b$ in equations (3.2) and (3.3) to obtain

$$a = F^{\frac{1}{3}}\left(\frac{DR}{2}\right)^{\frac{1}{3}} \qquad \text{--- equation (4)}$$

where F is the force in the contact region and $D = \frac{3}{2}(\frac{1-\sigma^2}{E})$. Substitution of equation (4) into equation (3.1) gives $h = F^{\frac{2}{3}}(\frac{D^2}{2R})^{\frac{1}{3}}$ which can be inverted to obtain the expression for the Hertzian force, $F \propto h^{\frac{3}{2}}$. [2]

1.2 Molecular adhesion between spheres:

The Derjaguin-Muller-Toporov model

The Hertizian force describes an ideal interaction in which adhesion between the spheres is not accounted for. The Derjaguin-Muller-Toporov (DMT) model[3] and the Johnson-Kendall-Roberts (JKR) model[4] are the most widely accepted theoretical models for the adhesive force that acts between spheres during contact. The JKR model is a more accurate approximation for large spheres with small stiffness which deform a lot during collision, while the DMT model works better for small spheres with large stiffness that deform relatively little[5]. Since our research deals with micrometer-scale stainless steel spheres which deform relatively little during impact, only the DMT model is presented here.

The DMT model is derived by considering the deformation of an elastic sphere in contact with a rigid surface. The energy of interaction between the sphere and the plane is decomposed into a sum of the volume energy of elastic deformations, $W_e = \int_0^\alpha F_e(\alpha)d\alpha$, and the surface energy of molecular forces, $W_s = \int_0^L \varphi(Z)2\pi r\, dr$ where $\varphi(Z)$ is the interaction energy per unit area. L can be taken to be infinity since for our relatively stiff spheres, $Z \ll R$. Note from the diagram that α is the deformation of the sphere and Z is the height of the deformed part of the sphere above the surface. [3]

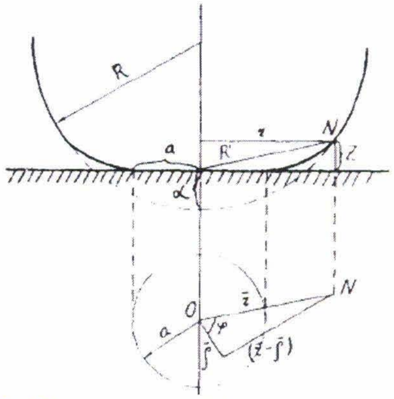

Fig 1.2a. Figure from ref [3] showing geometry being discussed.

In the region of contact, $Z = \varepsilon = constant$, where ε is the smallest possible spacing between the sphere's surface and the plane. Thus, the surface energy inside the contact region is $W_s' = \int_0^L \varphi(\varepsilon)2\pi r\, dr = \pi\alpha R\varphi(\varepsilon)$. Outside the region of contact the adhesive force still acts at a distance; in this region $(x,\alpha) = \frac{1}{\pi R}\left[ax + (x^2 - a^2)arctan\frac{x}{a}\right] + \varepsilon$. W_s'', the surface energy outside the region of contact, can be expressed as an integral depending on $Z(x,\alpha)$. Then, by the method of generalized displacements, the adhesive force at the place of contact is $F_s(\alpha = 0) = \frac{dW_s'}{d\alpha} + \frac{dW_s''}{d\alpha} = 2\pi R\varphi(\varepsilon)$. [3]

1.3 Dissipative forces

1.3.1 Dissipation during sliding motion

In classical models of friction, the dissipation of energy due to one material sliding against another is described by the Coulomb friction force $F_{cou} = -\mu N$, where N is the normal contact force. The value of the constant μ depends empirically on the materials in contact. When a force is applied to one of the materials, static friction initially acts between the materials. When the force exceeds a certain magnitude the material begins to slide against the other and Coulomb friction applies. The viscous drag force due to motion in fluids such as air or water follows the equation $F_{viscous} = -\frac{m}{T}v$. [6]

1.3.2 Dissipation during rotational motion

Attempts have been made to model dissipation due to rotational motion for both the JKR[7] and DMT[8] models. In particular, Brach, Dunn and Cheng derive a model for dissipation during rolling due to the tearing-off force required to overcome the molecular adhesion force derived in the DMT model.

They consider a rolling microsphere in contact with a flat surface. By considering the various torques on the sphere they arrive at the equation for angular displacement $mk^2\frac{d^2\theta}{d\tau^2} = -rF_t(\tau) + M_A(\tau) + M_H(\tau)$, where k is the radius of gyration and F_t is the tangential force on the sphere due to friction from the surface. The moment from the adhesion force which acts at the trailing edge of the contact during rolling is given by $M_A(\tau) = \int_0^{2\pi} f_0 C_A w a^3 \cos^2\alpha \, d\alpha = \pi f_0 C_A w a^3$, where f_0 is the adhesion force and C_A the adhesion dissipation constant. The moment due to the Hertzian deformation at the contact is given by $M_A(\tau) = \int_0^a \int_0^{2\pi} P(\rho', \alpha')\, C_H\, v_n(\rho', \alpha')\, \rho'^2 \cos\alpha' d\rho' d\alpha = \frac{K}{5}\sqrt{\frac{n}{R}} C_H w a^4$, where P is the Hertzian force, v_n is the relative velocity, C_H is the Hertzian dissipation constant and K is a constant depending on the Young's modulus and Poisson ratio. The geometry is labelled in fig 1.3.2a. [8]

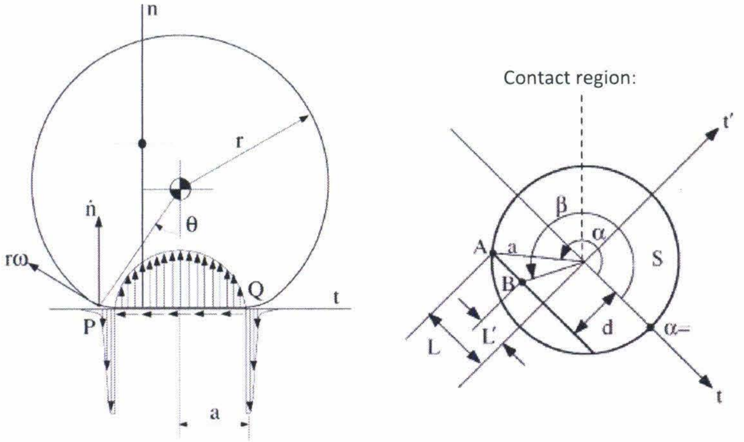

Fig 1.3.2a. Figure from ref 8] showing geometry being discussed.

1.4 The coefficient of restitution

Our current experimental setup can measure the positions and thus the velocities of the spheres, but is unable to resolve the deformation of the spheres during the collision and the adhesive forces at the surface of the spheres. We therefore need a way to extract information about the physics of the collision based solely on velocity data before and after the collision.

The coefficient of restitution provides a means by which this may be achieved. It is defined as $C_{res} = \frac{v_{2f} - v_{1f}}{v_{1i} - v_{2i}}$ where v_{2f} is sphere 2's velocity just after the collision, v_{1f} is sphere 1's velocity just after the collision, v_{1i} is sphere 1's velocity just before the collision and v_{2i} is sphere 2's velocity just before the collision. Although classical theory predicts that C_{res} should be a constant, experiments have shown that it tends to be a decreasing function of the impact velocity. The experiments of Antypov et al, and Kuwabara and Kono show it to be a monotonically decreasing function of the impact velocity[9],[10], whereas the experiments by King et al. have shown it to decrease non-monotonically[11].

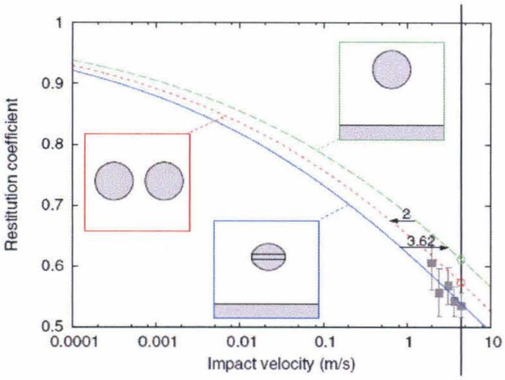

Fig 1.4a. Figure from Antypov et al (ref [9]) showing the experimentally measured coefficient of restitution decreasing monotonically as a function of impact velocity.

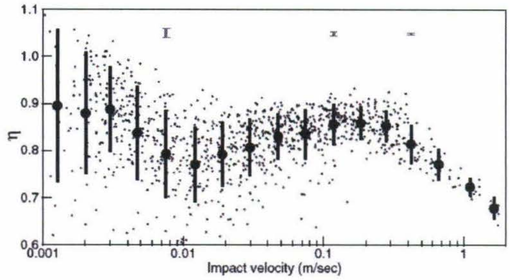

Fig 1.4b. Figure from King et al (ref [11]) showing the experimentally measured coefficient of restitution decreasing non-monotonically as a function of impact velocity.

There are numerous models attempting to explain the velocity dependence of the coefficient of restitution. One approach is to apply a viscoelatic collision model with adhesive forces based on the JKR model to derive a decreasing coefficient of restitution.[12] Another approach is to include a dissipative term that is proportional to the rate of change of deformation. In the work of Kuwabara et al and Morgado et al, the equation of motion for the deformation is $\frac{m}{2}\frac{d^2h}{dt^2} = -\frac{5}{4}kh^{\frac{3}{2}} - \frac{5}{2}k'\sqrt{h}\frac{dh}{dt}$ [11],[13]. The first term on the right-hand side is the Hertzian force and the second is the dissipative term.

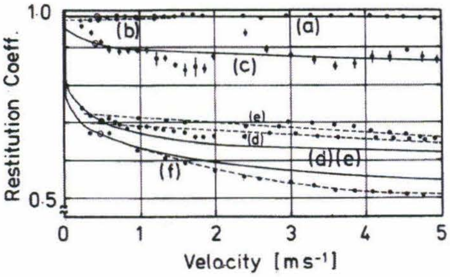

Fig 1.4c. Figure from Kuwabara et al (ref [10]). The solid curves are predicted by their model. The points are experimentally measure values of the coefficient of restitution.

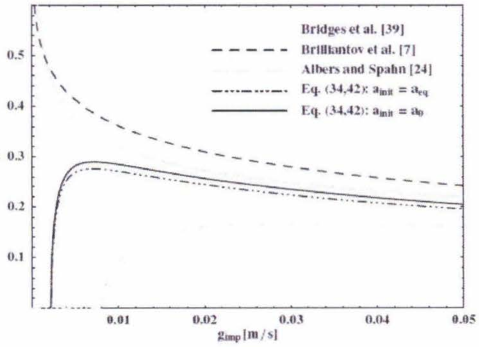

Fig 1.4d. Figure from Brilliantov et al (ref [12]) showing their predicted dependence of the coefficient of restitution on the impact velocity. Numerous other models from the literature are shown as well.

Given the preponderance of theoretical models, our approach is to experimentally investigate the velocity dependence of the coefficient of restitution for our system and then compare it with various models to determine which gives the best fit. When precise measurements of the coefficient of restitution are made we will be able to modify the terms in the theoretical model until it matches the experimental results. Thus, without measuring the details of the collision per se, we can verify theoretical models that predict the experimental observable- the coefficient of restitution- and thus understand the physics of the collision.

2. Experiments

2.1 Overview of experiments

The goal of the experiments is to study the dynamics of one-dimensional collisions between micrometer-scale spheres. The spheres are placed in a v-shaped groove fabricated on a silicon wafer which maintains their alignment throughout the collision process and restricts their motion to one dimension. A sphere is excited into motion by a laser pulse which ablates material from the sphere's surface. The reaction force from the ablation pushes the sphere forward. The motion of the spheres is captured using a high-speed camera, and their displacement-time data is extracted via image processing of the footage. Curve fitting of the data is then used to extract parameters of interest.

Before and after the collision, the parameters of interest include the air resistance friction coefficient and the coefficient of friction between the sphere and the groove. During the collision the coefficient of friction between the two spheres in contact becomes important as well. In addition, the coefficient of restitution $C_{res} = \frac{v_{2f} - v_{1f}}{v_{1i} - v_{2i}}$, a ratio of the difference between the two spheres' final and initial velocities, provides inside into the dissipative losses that occur during the collision.

2.2 Experimental materials

2.2.1 Stainless steel spheres

The two types of spheres used in our experiments were made of grade 440C (SS 440C) and grade 316C (SS 316C) stainless steel. The SS 440C spheres have a diameter of 229μm and a mass of 47.9μg. The SS 316C spheres have a diameter of 300μm and a mass of 113μg. The two different sizes were chosen in order to study how sensitive the results would be to the mass and size of the spheres.

2.2.2 Grooves on silicon wafers

The grooves in which the spheres were placed were fabricated on silicon wafers via anisotropic wet chemical etching. A 1μm thick layer of silicon nitride (Si_3N_4), designed to act as a mask, was deposited on the surface of [100] silicon wafers via chemical vapor deposition. Patterns corresponding to the desired groove dimensions were etched into the Si_3N_4 mask via photolithography and reactive-ion etching processes. The grooves were then etched into the unmasked silicon using a 50% KOH solution at

85°C. The grooves had a width of 240μm and a groove angle of 70.6°, with an estimated surface roughness of ~ 0.1 μm[15]. [14]

2.3 Experimental setup

The spheres are excited into motion by a Q-switched Nd:Yag nanosecond laser (Quantel Brilliant, maximum power 3.2W, 532nm wavelength, pulse duration 4ns) operating at various laser intensities. The laser beam is channeled through a half-wave plate and a polarized beam splitter. The beam splitter splits the beam into two arms. The groove wafer is positioned and clamped onto a sample stage such that one arm of the beam is aligned with the front end of the groove and the other with its back end. By rotating the halfway plate we can change the polarization of the beam, and thus control the beam intensity on each arm. [14] For the experiments presented here, we only use the front arm of the beam.

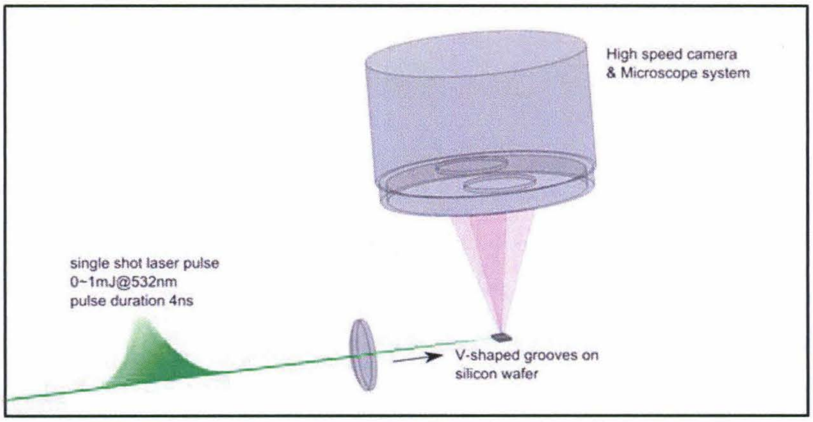

Fig 2.3a. Schematic of experimental setup. Spheres are placed in a v-shaped groove etched into a silicon wafer. A laser pulse is fired at the first sphere. The sphere's motion is captured by the high-speed camera. Image courtesy of ref [14].

The spheres are placed inside the groove by hand using tweezers and moved to precise initial positions via a robotic positioning system. The positioning system consists of a positioning tip (fine steel wire glued to a 3d-printed plastic tip) whose motion is controlled in 3 perpendicular directions, x, y and z, by 3 motors. The groove lies in the x-y plane, parallel to the x-axis. The positioning system's software makes use of images from the high-speed camera and image processing to locate the spheres. At the beginning of each experiment, the system locates the spheres using image deconvolution. It then brushes the spheres from above until they are 100 pixels apart from each other. Next, it pushes each sphere to the desired initial position, which is specified in pixels by the user.

The front arm of the laser beam is focused via a lens onto the center of the first sphere. A laser pulse 4ns in duration is fired at the sphere. The size of the laser spot on the sphere's surface is 40 μm. [14] The laser pulse ablates a thin layer of material from the sphere's surface, resulting in reaction forces that push the sphere forward in the groove[16].

A high-speed camera (Phantom v12.1) is used to image the motion of the spheres. The image of the spheres to be recorded is magnified by a Leica S6D microscope with additional achromatic lens sets between the camera and the sample stage. The microscope setup provides a spatial resolution of 4.3µm per pixel, and the maximum field of view is 5.5x3.4mm^2. The high-speed camera is operated at 25000fps with a 39µs exposure time and a total pixel resolution of 960x120. A 150W quartz halogen fiber optic illuminator (Fiber-Lite PL800 150W) is used to illuminate the sample stage. [14]

For the data analysis, the positions of the spheres on the groove at each point in time are retrieved from the saved images through image deconvolution. [14] Curve fitting of the displacement-time graphs is used to extract the experimental parameters of interest.

2.4 Experiments conducted

We began by conducting experiments for single spheres moving in a groove using both the SS 440C and the SS 316C spheres. However, when we moved on to collisions between two spheres, we were unable to obtain results for the SS 440C spheres because they tended to stick to the positioning tip and thus be lifted out of the groove. Despite our efforts to electrically ground the tip to prevent the spheres from sticking to it due to static electricity, the problem persisted. The problem is therefore probably due to adhesive forces between the sphere's surface and the tip. This problem does not occur for the heavier SS 316C spheres, whose weight probably overcomes the adhesive force, preventing them from being lifted out of the groove. Thus, the two-sphere collision experiments were performed with SS 316C spheres only. Future improvements to the experimental system will be required in order to perform the collision experiments with SS 440C spheres so as to study how the collision physics may vary with sphere mass and size.

2.4.1 Precision of automated sphere positioning system

This initial experiment was designed to test the precision of the automated robotic sphere positioning system. First, the system was programmed to position a single sphere in a groove at a target x-coordinate of 200 pixels. The positioning test was repeated 100 times. Next, the system was programmed to push a sphere to the left 30 times in target increments of 5 pixels per push. Results from this test give indicate how precisely the robotic system can move a sphere to a desired position or move it by a desired number of pixels.

2.4.2 Single spheres moving in a groove (SS 440C and SS 316C)

The purpose of this experiment is to determine the air resistance friction coefficient and sphere-groove friction coefficient for SS 316C and SS 440C spheres. A single sphere (SS 316C or SS 440C) was placed in a v-groove and excited by a 4ns laser pulse at various laser energies. The range of laser energies was used to create a range of initial velocities.

The SS 316C spheres were excited with a 4ns laser pulse at 14 different laser energies. The experiment was repeated 15 times per laser energy, making for a total of 210 runs of the experiment. The laser energies used were 0.151, 0.215, 0.244, 0.275, 0.300, 0.302, 0.322, 0.324, 0.342, 0.355, 0.356, 0.363, 0.364 and 0.366 mJ/pulse.

The SS 440C spheres were excited with a 4ns laser pulse at 14 different laser energies. The experiment was repeated 15 times per laser energy, making for a total of 210 runs of the experiment. The laser energies used were 0.0222, 0.0385, 0.0587, 0.0590, 0.108, 0.135, 0.164, 0.192, 0.219, 0.245, 0.268, 0.287, 0.304 and 0.315 mJ/pulse. The laser energies used for SS 440C were lower than those used for SS 316C because of the lower mass of the SS 440C spheres, which allowed this range of laser energies to produce the same range of initial velocities as for SS 316C.

The displacements of the spheres at each point in time were recorded using the high-speed camera.

2.4.3 Collision between two spheres in a groove (SS 316C)

The goal of the collision experiment is to extract the coefficient of restitution and sphere-sphere friction coefficient for SS 316C. Two SS 316C spheres were positioned at an initial distance of 300 pixels apart by the robotic positioning system. The first sphere was excited with a 4ns laser pulse at 10 different laser energies. The experiment was repeated 20 times per laser energy, giving a total of 200 runs of the experiment. The laser energies used were 0.122, 0.140, 0.165, 0.189, 0.212, 0.233, 0.251, 0.265, 0.276

and 0.283 mJ/pulse. The first sphere collided with the second sphere, which was initially stationary. The displacements of the spheres at each point in time were recorded using the high-speed camera.

2.4.4 Improved collision experiment between two spheres in a groove (SS 316C)

In the earlier collision experiment, the first sphere was excited into motion by direct laser ablation. The damage to the sphere's surface due to the ablation may have affected the results. To improve, we instead used a third 'striker' sphere to excite the first sphere into motion, such that only the third sphere was shot by the laser. Of interest in this experiment is the collision between the first and second spheres. Displacement-time data from the striker sphere is not used.

The first and second spheres were again positioned 300 pixels apart by the robotic positioning system. The striker sphere was positioned 100 pixels away from the first sphere. The striker sphere was excited into motion by a 4ns laser pulse at 10 different laser energies. The laser energies used were 0.115, 0.152, 0.191, 0.211, 0.232, 0.253, 0.273, 0.293, 0.313 and 0.351 mJ/pulse. The experiment was repeated 20 times per laser energy, giving a total of 200 runs of the experiment. Upon being hit by the striker, the first sphere was set into motion and collided with the second sphere. The displacements of the spheres at each point in time were recorded using the high-speed camera.

3. Results and Discussion

3.1 Precision of automated sphere positioning system

3.2 Single spheres moving in a groove (SS 316C and SS 440C)

3.2a) Least- squares fits of displacement-time graphs

3.2b) Physical explanation

3.2c) Transition time, t_T

- **3.2.1 Determining the air resistance friction coefficient, T**
- **3.2.2 Determining the sphere-groove Coulomb friction coefficient, μ_g**

3.3 Collision between two spheres in a groove (SS 316C)

3.3a) Least- squares fits of displacement-time graphs

- **3.3.1 Determining the sphere-sphere friction coefficient, μ_b**
- **3.3.2 Determining the coefficient of restitution, C_{res}**

3.4 Improved collision experiment between two spheres in a groove (SS 316C)

- **3.4.1 Determining the sphere-sphere friction coefficient, μ_b**
- **3.4.2 Determining the coefficient of restitution, C_{res}**

3.1 Precision of Automated Sphere Positioning System

The robotic sphere positioning system is able to position a sphere at a desired location with great precision. Figure 1a) shows that the sphere was positioned precisely at the desired x-coordinate of 200 pixels in all but 3 out of 100 trials. Figure 1b) shows that the sphere was pushed to the left by precisely five pixels in all but 2 out of 30 trials. The 2 'bad' trials were caused by the sphere sticking to the positioning tip and being pulled back to the tip's resting position. The problem of spheres sticking to the tip was reduced by changing the material of the tip to stainless steel and electrically grounding it to prevent the buildup of static charge.

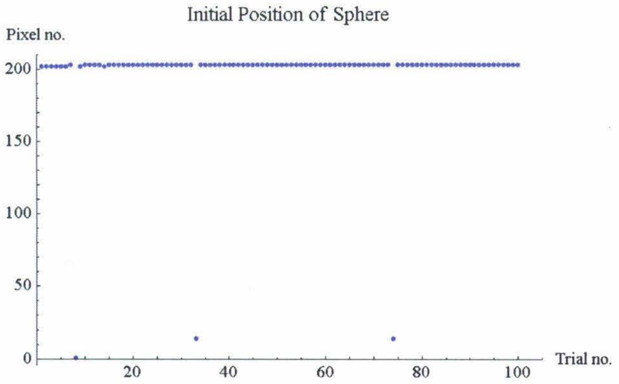

Fig 3.1a. The robotic positioning tip was able to precisely position the sphere at the desired pixel number 200 in 97 out of 100 trials.

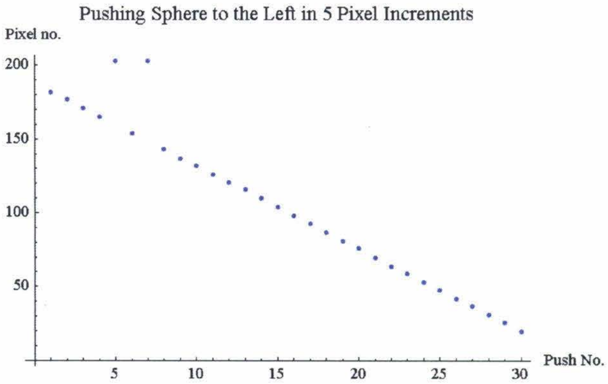

Fig 3.1b. The robotic positioning tip was able to push the sphere to the left by precisely 5 pixels in 28 out of 30 trials. In the remaining 2 trials the sphere stuck to the tip and was dragged back to the tip's resting position. The problem of spheres sticking to the tip was reduced by electrically grounding the tip.

3.2 Single spheres moving in a groove (SS 316C and SS 440C)

3.2a) Least- squares fits of displacement-time graphs

A typical displacement-time profile contains an initial quadratic part followed by an exponential part. Using least-squares fitting we determined that the exponential part obeys the equation $x = a + bT(1 - e^{\frac{-t}{T}})$ and that the initial quadratic part obeys the equation $x = x_0 + v_0 t + ct^2 + a + bT(1 - e^{\frac{-t}{T}})$.

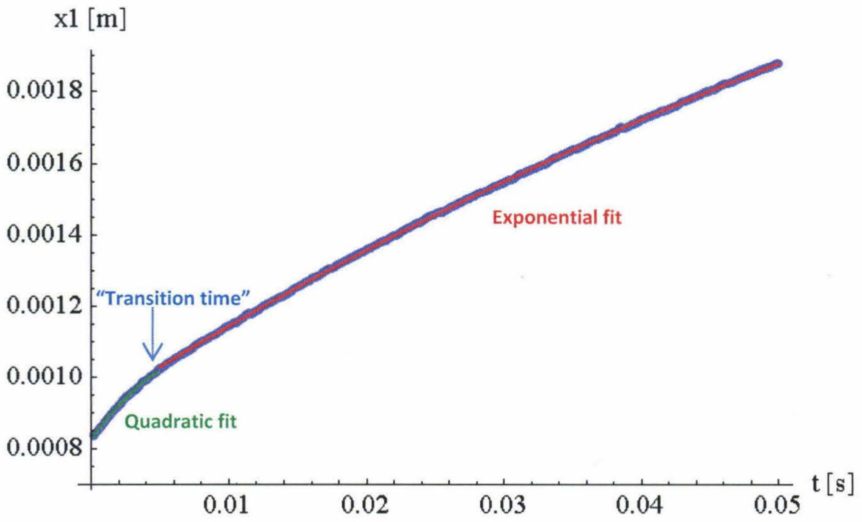

Fig 3.2a)-1.Typical displacement-time graph for a bead rolling in a groove. An initial quadratic part and a subsequent exponential part can be distinguished by performing least-squares fits on the data. We define the "transition time" as the time when the graph shape changes from quadratic to exponential.

The exponential part corresponds to deceleration due to air resistance, given by $F_{air} = m\frac{d^2x}{dt^2} = -\frac{m}{T}\frac{dx}{dt}$ where T is the friction coefficient corresponding to air resistance. T can be directly found from the exponential fit. The quadratic part corresponds to constant deceleration due both to F_{air} and to the Coulomb friction force $F_{cou} = m\frac{d^2x}{dt^2} = \mu_g N$, where μ_g is the Coulomb friction coefficient and $N = 2mg\, sin\theta_0\, cos\theta_0$ is the normal contact force acting on a sphere sitting in a groove with groove angle θ_0. The displacement corresponding to F_{cou} is given by $x = x_0 + v_0t + ct^2$. Differentiation of this expression yields $\frac{d^2x}{dt^2} = 2c$. Inserting this into the expression for F_{cou} we obtain an expression for μ_g in terms of c, $\mu_g = -\frac{2c}{g\, sin\theta_0}$, which enables us to determine μ_g from the quadratic fit. The "transition time", which we define as the time when the displacement-time curve changes from quadratic to exponential, can be precisely determined as the intersection point of the quadratic and exponential fits.

A typical set of quadratic and exponential fits together with their residuals are shown below. Residuals were typically small in magnitude (of the order of 10^{-6}) and randomly distributed about 0, indicating that the fits were appropriate. In addition, fit parameters did not change drastically between runs of the experiment, indicating that the fits were appropriate for the data.

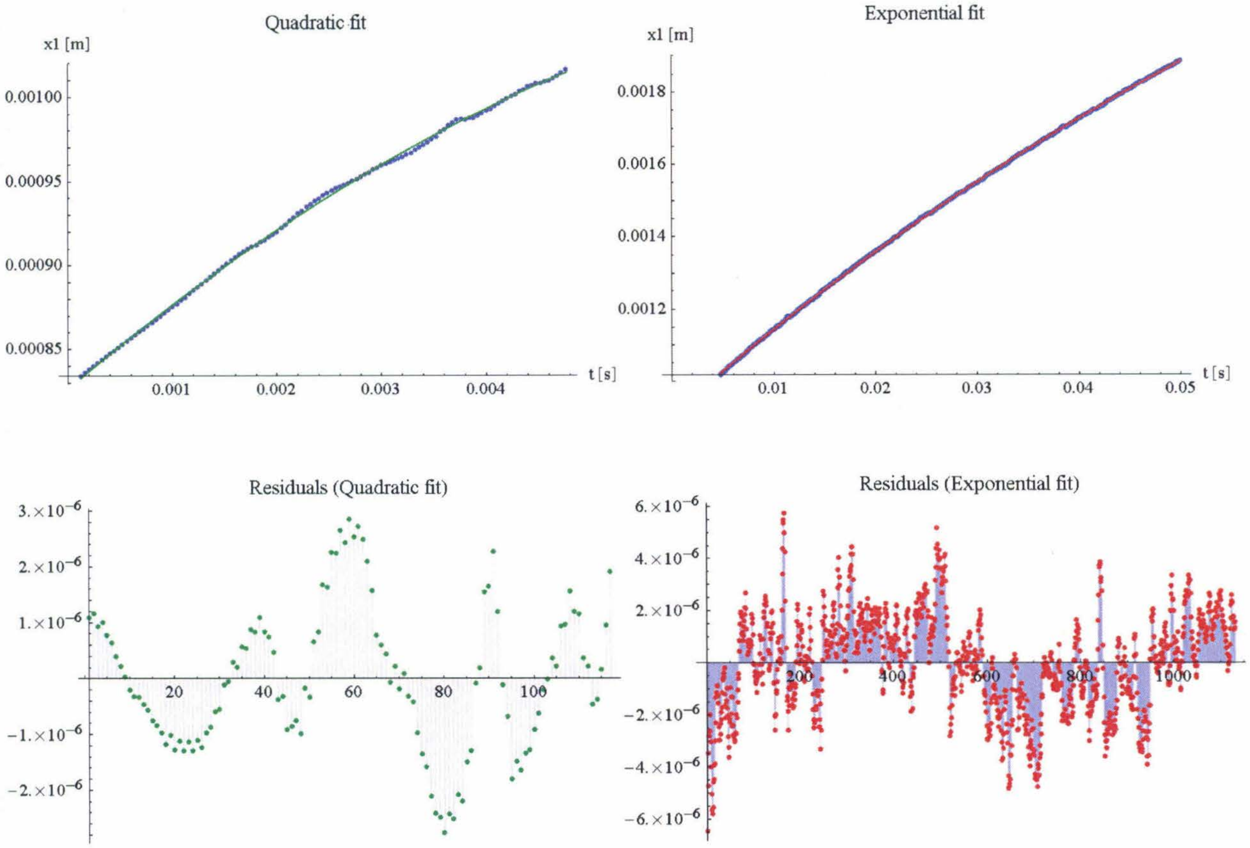

Fig 3.2a)-2. Typical quadratic and exponential fits with residuals shown. The small magnitude and random distribution of the residuals, as well as the consistency of fit parameters between different runs of the experiment, indicate that the fits were appropriate.

3.2b) Physical explanation

We can provide a physical explanation for the presence of two parts- quadratic and exponential- in the displacement-time graphs. After laser excitation, the sphere initially slips on the groove. In accordance with the Coulomb model, kinetic friction acts between the sphere's surface and the groove's surface as the former slides against the latter, thus producing displacement which depends quadratically on time. Air resistance also acts on the sphere at this time since it has non-zero velocity.

At the transition time, the sphere stops sliding and begins to roll without slipping. This occurs when the point of contact between the sphere and the groove is stationary. Thus, at the transition time, the sphere has slowed to the point where its velocity v is equal to srw, where $s = \sin(\frac{\theta_0}{2})$ and θ_0 is the groove angle. During rolling without slipping no kinetic friction acts between the sphere and the groove, so only the effect of air resistance is left. The air resistance produces displacement which varies exponentially in time, as expected.

<u>3.2c) Transition time, t_T</u>

The transition time t_T , which is the time when the sphere stops sliding and begins to roll without slipping, is plotted as a function of initial velocity v_0 for SS 316C and SS 440C spheres respectively. t_T increases with v_0, as is to be expected since spheres imparted with a greater initial velocity should slip for a longer time. For both types of spheres, t_T appears to be a linear function of v_0. For SS 316C spheres, the linear fit is t_T= -$(0.00177 \pm 0.00063\ ) + (0.192 \pm 0.011)v_0$. For SS 440C spheres, the fit is given by $t_T = (0.00161 \pm 0.00059) + (0.148 \pm 0.014)v_0$. Ideally, these graphs would allow us to predict when a sphere with a given initial velocity will start rolling without sliding. A comparison of this data with theoretically predicted transition times (based on models including the air resistance and Coulomb friction) could be used to verify theoretical models. However, for the SS 316C fit the value of the adjusted coefficient of determination R-squared is 0.579, and for the SS 440C fit it is 0.489. The R-squared values are not very close to 1, most likely due to the large scatter of data points about the best fit line, particularly in the case of SS 440C. More precise transition time data is needed to conclude about the dependence of transition time on initial velocity.

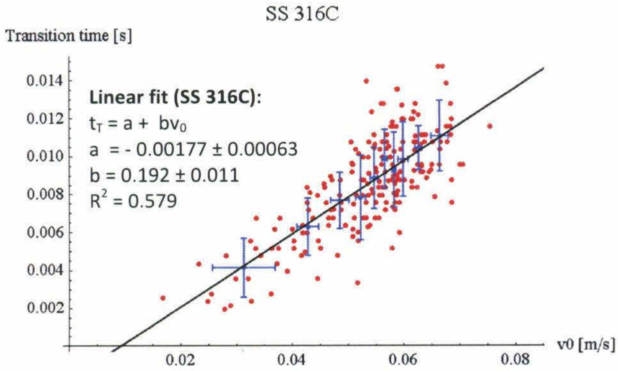

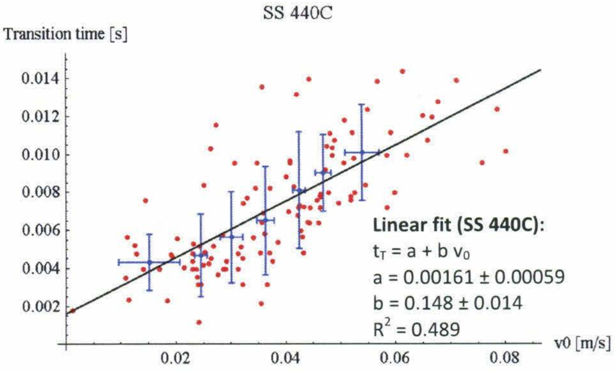

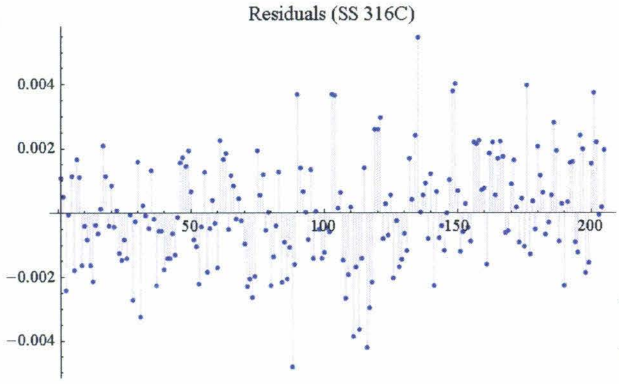

Fig 3.2c)-1. Transition time t_T as a function of v_0, the initial velocity of the sphere, for SS 316C spheres. The transition time increases linearly with v_0, matching the linear fit $t_T = -(0.00177 \pm 0.00063) + (0.192 \pm 0.011)v_0$. However, $R^2 = 0.579$ which is not close to 1.

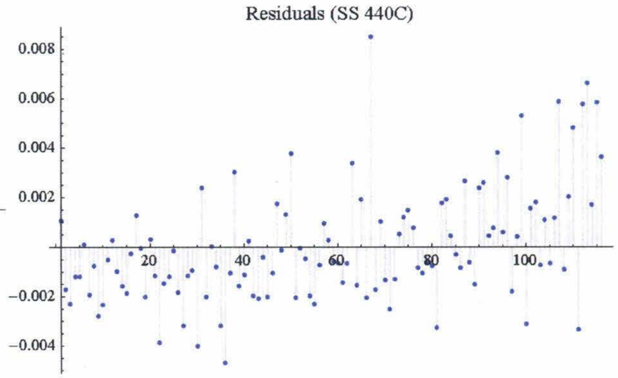

Fig 3.2c)-2. Transition time t_T as a function of v_0, the initial velocity of the sphere, for SS 440C spheres. The transition time increases linearly with v_0, matching the linear fit $t_T = (0.00161 \pm 0.00059) + (0.148 \pm 0.014)v_0$. However, $R^2 = 0.489$ which is not close to 1.

3.2.1 Air resistance friction coefficient, T

The air resistance coefficients T determined from the 210 runs of the experiment with SS 316C stainless steel spheres and the 210 runs of the experiment with SS 440C stainless steel spheres are plotted as a function of the initial velocity of the sphere, v_0. For SS 316C, T is approximately constant at $T = 0.0959 \pm 0.0056\ s$ at low velocities and begins to increase at higher velocities. At higher velocities we observe an increased spread in the values of T. For SS 440C spheres, T gradually increases with v_0. Although the numerical values of T for SS 316C and SS 440C fall within a similar range, the velocity dependence is quite different, suggesting that the differences in masses of SS 316C (113μg) and SS 440C (47.9μg) and the difference in their surface areas (2.83×10^{-7} m^2 for SS 316C versus $1.65\times10^{-7} m^2$ for SS 440C) do influence the air resistance acting on the spheres.

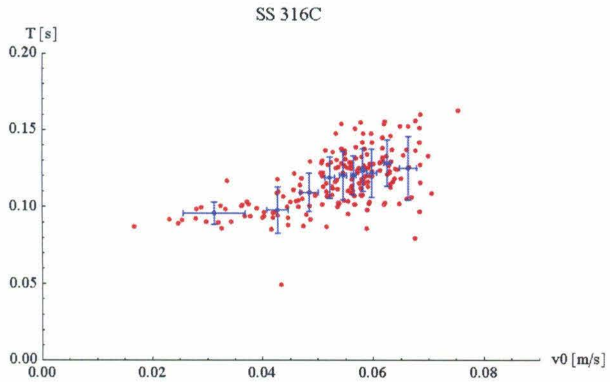

Fig 3.2.1a. Air resistance friction coefficient T as a function of v_0, the initial velocity of the sphere, for SS 316C spheres. T is approximately constant at T = $0.0959 \pm 0.0056\ s$ for low velocities, and begins to increase at higher velocities.

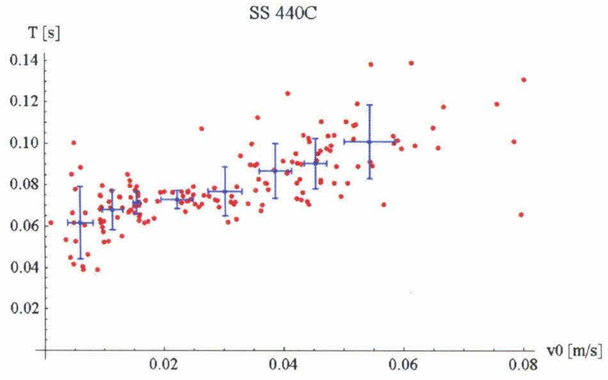

Fig 3.2.1b. Air resistance coefficient T as a function of v_0, the initial velocity of the sphere, for SS 440C spheres. T increases gradually with v_0.

3.2.2 Sphere-groove Coulomb friction coefficient, μ_g

The Coulomb friction coefficient μ_g , which describes the friction between the sphere and the groove when the sphere is sliding on the groove, is plotted as a function of the initial velocity of the sphere for SS 316C and SS 440C spheres. For SS 316C spheres, μ_g remains constant as initial velocity increases. The mean value of μ_g is 0.333 ± 0.065. On the other hand, for SS 440C spheres μ_g appears to increase gradually with initial velocity and then plateau out.

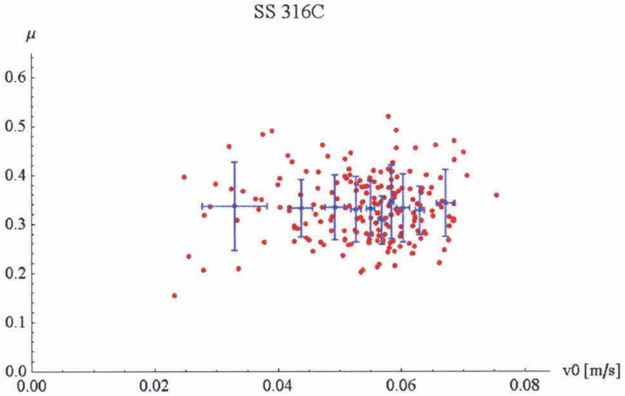

Fig 3.2.2a. Coulomb friction coefficient μ as a function of v_0, the initial velocity of the sphere, for SS 316C spheres. μ_g remains constant as v_0 increases, and has a value of 0.333 ± 0.065.

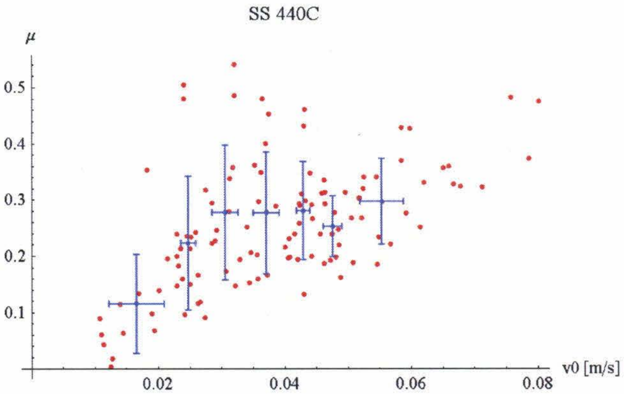

Fig 3.2.2b. Coulomb friction coefficient μ as a function of v_0, the initial velocity of the sphere, for SS 440C spheres. μ_g increases gradually with v_0 and then plateaus out.

3.3 Collision between two spheres in a groove (SS 316C)

3.3a) Least- squares fits of displacement-time graphs

A typical displacement-time graph for the two spheres is shown in fig 3a)-1. Sphere 1 is the 'striker' sphere which is excited by the laser pulse. For sphere 1, before the collision we can observe that the graph contains the expected initial concave quadratic part corresponding to sliding and the following exponential part corresponding to rolling without sliding. The collision point is demarcated by a drop in velocity which manifests as a decrease in the

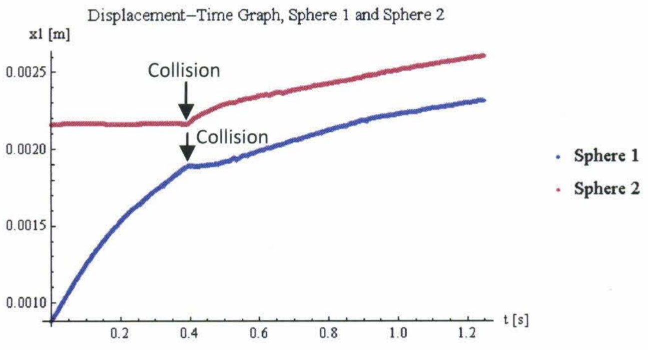

Fig 3.3a)-1. Displacement versus time graphs for each of the two spheres. Sphere 1 (blue line) is the 'striker' sphere which is set into motion by the laser pulse. Sphere 2 (red line) is initially at rest and begins to move after sphere 1 collides with it.

gradient of the displacement-time graph. Just after the collision, there is a convex quadratic region which obeys the equation $x = x_1 + v_1 t + c_1 t^2 + a + bT(1 - e^{\frac{-t}{T}})$, where the fit coefficients are different than for the initial concave quadratic part (see fig 3.1a for details). After the convex quadratic region there is again an exponential part corresponding to rolling without sliding.

Sphere 2 is initially at rest until it is hit by the striker. Its velocity is zero prior to the collision. After the collision its displacement-time graph contains the concave quadratic part corresponding to sliding and the exponential part corresponding to rolling with sliding.

3.3.1 Sphere-sphere friction coefficient, μ_b

Of particular interest in this experiment is the displacement-time profile of sphere 1 immediately after the collision, which is a convex quadratic obeying $x = x_1 + v_1 t + c_1 t^2 + a + bT(1 - e^{\frac{-t}{T}})$. The equation $x_1 + v_1 t + c_1 t^2$ describes acceleration rather than deceleration. We deduce that the acceleration arises because $sr\omega > v$ after the collision.

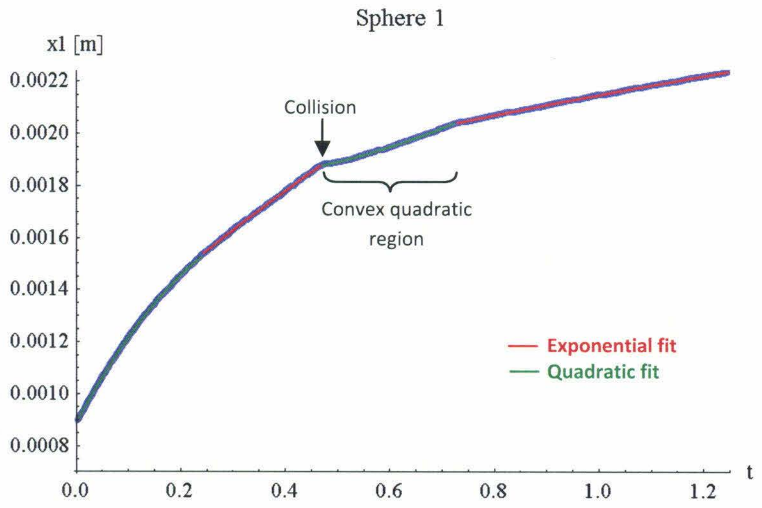

Fig 3.3.1a. Displacement-time profile of sphere 1. The convex quadratic region after the collision corresponds to acceleration, which arises because $sr\omega > v$ after the collision.

Each of the exponential and quadratic fits, together with their residuals, is shown in fig 3.1b. The overall random distribution of residuals about zero and the small size of the residuals indicate a generally good fit. In addition, the fit parameters did not vary drastically between different runs of the experiment, indicating that the fits were appropriate for the data.

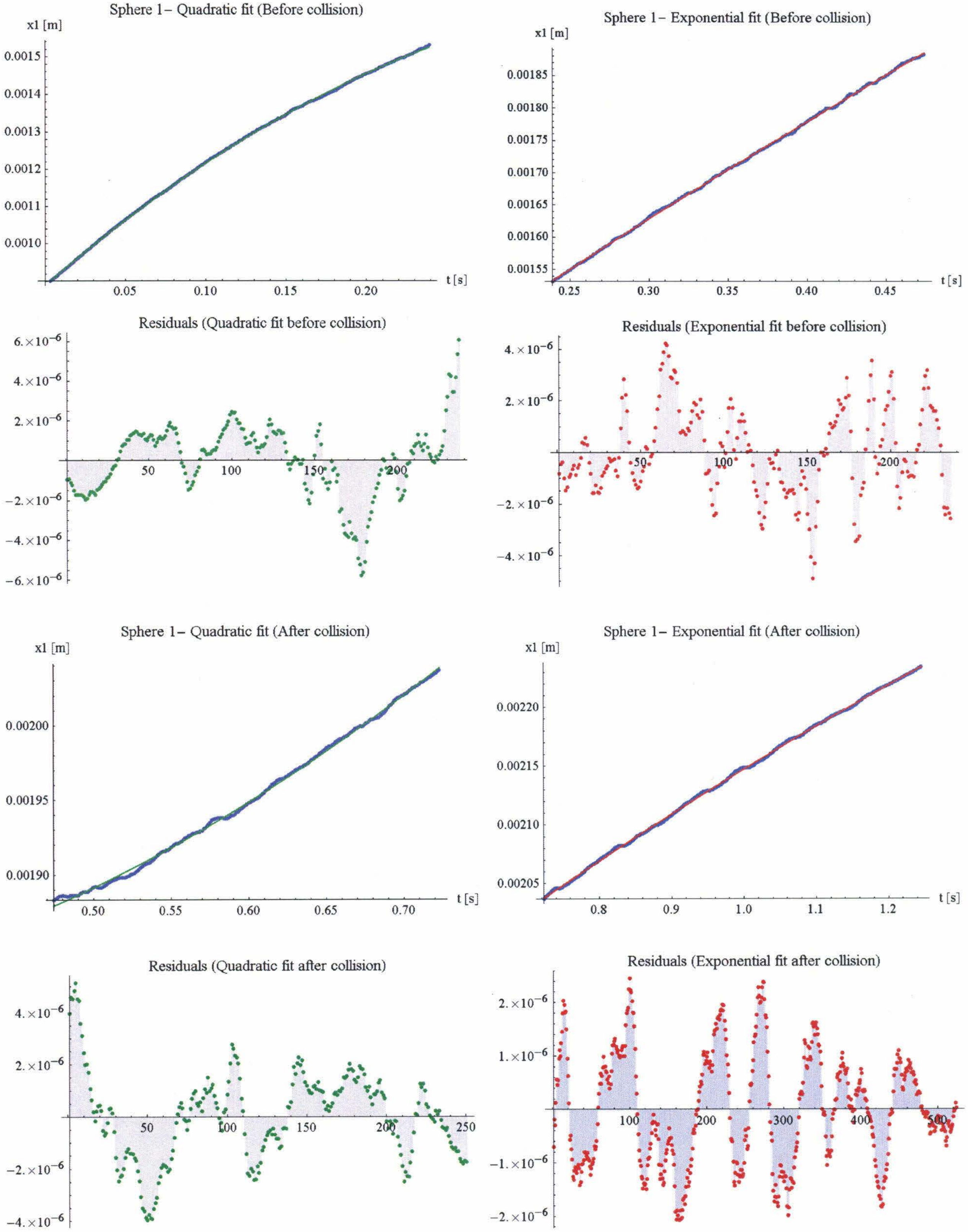

Fig 3.3.1b. Example of quadratic and exponential fits to sphere 1's displacement-time data before and after the collision. The residuals and consistency of fit parameters between runs of the experiment indicate an appropriate fit.

By considering $\frac{dv}{dt} = -\frac{g\mu_g}{s}$ and $r\frac{dw}{dt} = kg\mu_g$ over a period of time Δt, we arrive at the relation $srw_i = (ks^2 + 1)v_f - ks^2 v_i$, where k = 5/2 is related to the moment of inertia of the sphere, v_i and w_i are the initial linear and angular velocities of the sphere and v_f is the final linear velocity of the sphere. Δv and Δw can thus be determined simply from fit data which gives the velocities of the sphere before the collision, just after the collision and at the end of the convex quadratic part. In addition, we have that $-\Delta v = \int \frac{F_{cou}}{m} dt = \int \frac{\tau}{\mu_b r m} dt = -\frac{r\Delta w}{k\mu_b}$ and so $\Delta w = \frac{\mu_b k}{r}\Delta v$, where r is the sphere radius and μ_b is the friction coefficient between the two spheres.

Thus, a plot of Δw against Δv for sphere 1 yields the sphere-sphere friction coefficient, μ_b. From a linear fit of the graph we obtain $\mu_b = 1.403 \pm 0.046$. The adjusted value of the coefficient of determination R-squared for the fit is 0.852 which is close to one, indicating that the linear fit is appropriate.

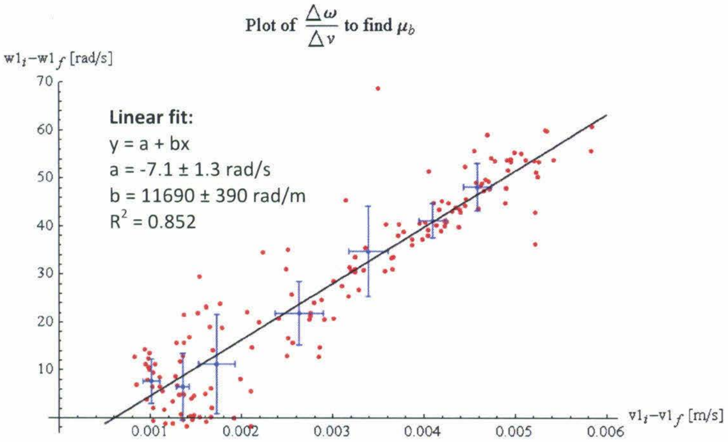

Fig 3.3.1c. Plot of Δw vs Δv for sphere 1, the striker sphere. Since $\Delta w = \frac{\mu_b k}{r}\Delta v$, μ_b can be obtained from a linear fit of the data. Its value is $\mu_b = 1.403 \pm 0.046$.

The black line is the linear fit y = a + bx where a = -7.1 ± 1.3 rad/s and b = 11690 ± 390 rad/m. The R-squared value of the fit is R^2 = 0.852 which is close to 1, indicating that the linear fit is appropriate.

3.3.2 Coefficient of restitution, C_{res}

The coefficient of restitution is given by $C_{res} = \frac{v_{2f} - v_{1f}}{v_{1i} - v_{2i}}$ where v_{2f} is sphere 2's velocity just after the collision, v_{1f} is sphere 1's velocity just after the collision, v_{1i} is sphere 1's velocity just before the collision and v_{2i} is sphere 2's velocity just before the collision. It can be calculated directly from the velocities obtained from curve fitting. It is plotted here as a function of $v01$, which is the velocity of sphere 1 at the start of the experiment just after it has been excited by the laser pulse.

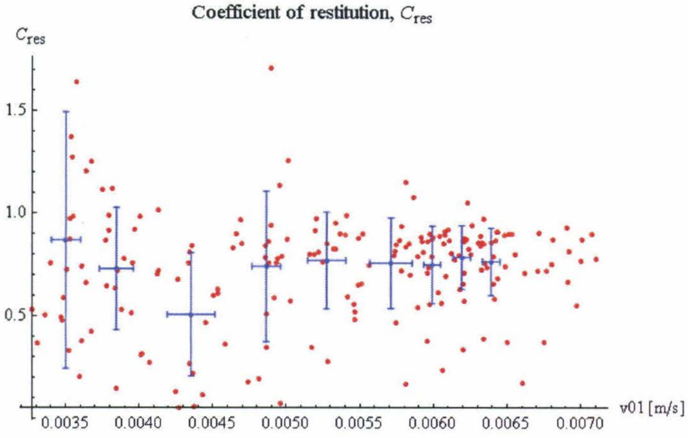

Fig 3.3.2a. Plot of C_{res}, the coefficient of restitution, against $v01$, the velocity of sphere 1 at the beginning of the experiment just after it has been excited by the laser pulse. C_{res} = 0.73 ± 0.27, which indicates that the data is too noisy and cannot be used to determine C_{res}.

C_{res} appears to be constant in $v01$, but a calculation of the mean and standard deviation of C_{res} yields $C_{res} = 0.73 \pm 0.27$. The magnitude of the standard deviation is 37% of the magnitude of the mean. Thus the data is too noisy to allow for a precise determination of C_{res} . Data from other sets of experiments were also used to calculate C_{res}, and in all cases, C_{res} could not be precisely determined. A future improvement to the experimental setup will be required in order to investigate the dependence of C_{res} on $v01$ and to precisely determine C_{res} .

It is notable that several values of C_{res} are larger than 1. At first glance, this seems to indicate that kinetic energy has been generated, rather than dissipated, in the collision. However, coefficients of restitution larger than 1 have been observed in the case of oblique collisions impacts of hard aluminum oxide spheres on thick elastoplastic polycarbonate plates. This has been attributed to a change in the effective normal between the sphere and the plate, which arises due to deformation of the plate and is not captured in the calculations for the restitution coefficient, rather than to an increase in the total kinetic energy.[17] In our system, however, oblique impact is prevented by the groove. It is likely that our C_{res} values larger than 1 arise instead because some of the spheres' angular momentum is converted into linear momentum during the collision, as is observed in the convex quadratic part of sphere 1's displacement-time graph right after the collision which indicates that sphere 1 is accelerating due to torque from sphere 2. Since the coefficient of restitution accounts for linear momentum only, the non-zero angular momentum of our spheres is probably the cause of the 'anomalous' C_{res} values which are larger than 1.

3.4. Improved collision experiment between two spheres in a groove (SS 316C)

In this improved collision experiment, a third sphere rather than a direct laser pulse was used to excite sphere 1 into motion in order to avoid damaging the surface of sphere 1 due to laser ablation. The displacement-time graphs for this experiment were qualitatively identical to experiment 3.3 and are therefore not shown here. The third sphere was merely used as a striker, so its displacement-time data was not used. Both sphere 1 and sphere 2 showed the same quadratic regions corresponding to sliding on the groove and the exponential regions corresponding to rolling without sliding. Sphere 1's graphs showed the same convex quadratic region corresponding to acceleration after the collision as before. Curve-fitting was carried out using the same equations as in experiment 3.3.

3.4.1 Sphere-sphere friction coefficient, μ_b

A graph of Δw against Δv was again generated to find the sphere-sphere friction coefficient, μ_b, from the relation $\Delta w = \frac{\mu_b k}{r} \Delta v$. A linear fit of this data gives $\mu_b = 1.341 \pm 0.021$. To compare this with the value found in experiment 3.3, compute the quantity $= \frac{|\mu_3 - \mu_4|}{\sqrt{\sigma_3^2 - \sigma_4^2}}$. If $\eta \leq 3$ we conclude that the two measurements, μ_3 and μ_4, agree since they are within 3 standard deviations of each other. $\eta = 1.23 < 3$, so we conclude that the value of μ_b found from experiment 3.4 is in good agreement with that found from experiment 3.3.

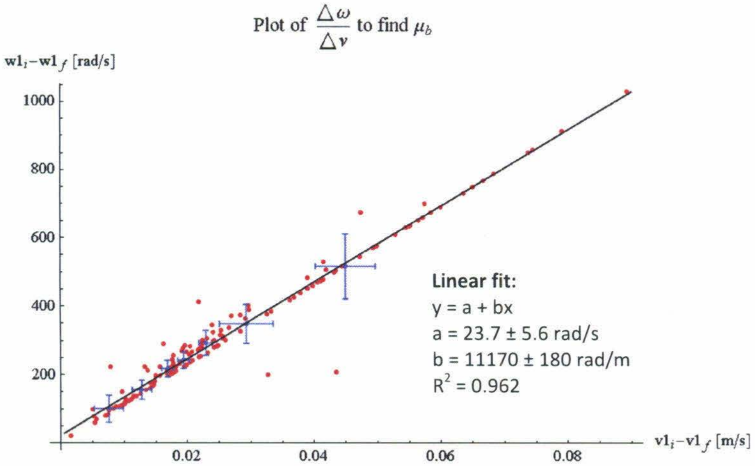

Fig 3.4.1a. Plot of Δw vs Δv for sphere 1, which was excited via impact by a third sphere. Since $\Delta w = \frac{\mu_b k}{r} \Delta v$, μ_b can be obtained from a linear fit of the data. Its value is $\mu_b = 1.341 \pm 0.021$, which agrees with the value found in experiment 3.3 with an η-value of 1.23 < 3.

The black line is the linear fit y = a + bx where a = 23.7 ± 5.6 rad/s and b = 11170 ± 180 rad/m. The adjusted R-squared value for the fit is 0.962 which is very close to 1, indicating that the linear fit is appropriate.

The adjusted R-squared value is 0.962 which is close to 1, indicating that the linear fit is appropriate. The data points in this experiment are distributed much more closely to the best fit line than in experiment

3.3.1, which is reflected in the adjusted R-squared value which even closer to 1 than before. These results may indicate that the technique of preventing damage to sphere 1 from laser ablation by using a third sphere as a striker may produce more reproducible results. It is possible that the damage to sphere 1 from the laser ablation caused the greater scatter in results in experiment 3.3.

3.4.2 Coefficient of restitution, C_{res}

The data for C_{res} is for this improved experiment is shown in fig 4.2a). Values of C_{res} greater than 1 are still present, and in this experiment there are also several values of C_{res} that are less than 0. For the positive values of C_{res}, $C_{res,+} = 0.65 \pm 0.37$. The large size of the standard deviation relative to the mean indicates that the data is still too noisy and cannot be used to precisely determine C_{res} or extract its velocity dependence.

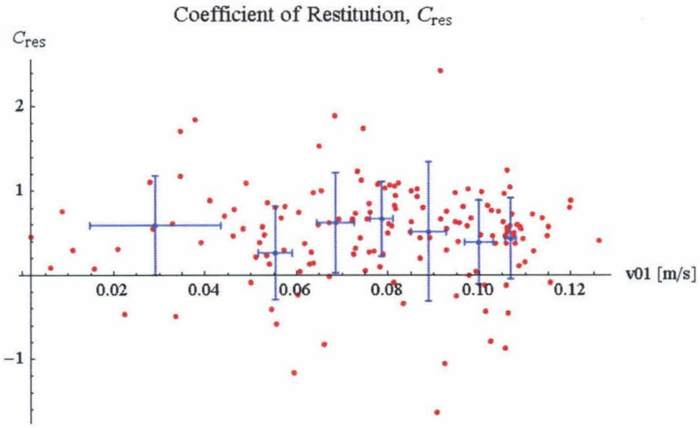

Fig 3.4.2a. Plot of C_{res}, the coefficient of restitution, against $v01$, the velocity of sphere 1 at the beginning of the experiment just after it has been excited into motion by the striker sphere. For the positive values of C_{res}, $C_{res,+}$ = 0.65 ± 0.37, which indicates that the data is still too noisy and cannot be used to determine C_{res}.

An examination of the data revealed that the negative values of $C_{res} = \frac{v_{2f} - v_{1f}}{v_{1i} - v_{2i}}$ here correspond to cases where the numerator, $v_{2f} - v_{1f}$, was negative. The denominator $v_{1i} - v_{2i}$ was always positive as expected. The convex quadratic region of sphere 1's displacement-time graph, as prominent in experiment 3.4 as it was in experiment 3.3, corresponds to linear acceleration of sphere 1 due to torque from sphere 2 during the collision. The negative denominators thus correspond to cases where sphere 1's velocity after the collision exceeded sphere 2's due to the linear acceleration from the torque.

4. Conclusion

This work has provided a first insight into the collision dynamics for micrometer-scale stainless steel spheres. The air resistance friction coefficients and Coulomb friction coefficients for SS 440C and SS 316C spheres have been experimentally determined. The sphere-sphere friction coefficient for SS 316C spheres has also been determined via two collision experiments whose results are in agreement. The coefficient of restitution for SS 316C spheres could not be precisely measured with the current experimental method and materials, and thus could not be compared with theoretical predictions. There was also a relatively large spread in transition times measured for SS 316C and SS 440C spheres, which would have to be improved on in order to compare these results with theoretical predictions of the transition time. Although efforts were already made to minimize contamination by dust, measurements might be improved by conducting the experiment in vacuum to prevent dust particles from affecting it. In addition, data from more different types of collisions (eg. collisions in which sphere 2 also has a non-zero initial velocity, glancing collisions in which the spheres collide at an angle) could be collected and cross-compared to confirm the experimental results.

5. References

[1] Henry D. I. Abarbanel; M. I. Rabinovich; M. M. Sushchik. (1993). *Introduction to Nonlinear Dynamics for Physicists.* World Scientific.

[2] Landau, L; Lifshitz, E. (1959). *Theory of Elasticity.* Pergamon Press. pp 30-36.

[3] Derjaguin, B.V.; Muller, V.M.; Toporov, YU.P. (1975). *Effect of Contact Deformations on the Adhesion of Particles.* J. Colloid Interface Sci. 53, pp 314-325.

[4] K. L. Johnson, K.L.; Kendall, K; Roberts, A.D. (1971). *Surface energy and the contact of elastic solids.* Proc. R. Soc. London A 324, pp 301-313.

[5] Peri, M.D.; Cetinkaya, Cetin. (2005). *Non-contact microsphere–surface adhesion measurement via acoustic base excitations*. Journal of Colloid and Interface Science 288, pp 432–443.

[6] Olsson, H et al. (1998). *Friction Models and Friction Compensation.* Eur. J. Control, Vol. 4, No. 3., pp 176-195.

[7] Dominic, C.; Tielens, A.G.G.M. (2004). *Resistance to Rolling in the Adhesive Contact of Two Elastic Spheres.* Philosophical Magazine A, 72:3, pp 783-803.

[8] Brach, R.M.; Dunn, P.F.; Cheng, W. (1999). *Rotational Dissipation During Microsphere Impact. J. Aerosol Sci*. Vol. 30, No. 10, pp 1321-1329.

[9] Antypov, D.; Elliott, J. (2011). *Effect of particle size on energy dissipation in viscoelastic granular collisions*. Physical Review E 00, 001300.

[10] Kuwabara, G.; Kono, K. (1987). *Restitution Coefficient in a Collision Between Two Spheres*. Japanese Journal of Applied Physics, Vol. 26, No. 8, pp 1230-1233.

[11] King, H. et al. (2011). *Inelastic impact of a sphere on a massive plane: Nonmonotonic velocity-dependence of the restitution coefficient*. EPL Vol 93, Number 1, Article 14002.

[12] Brilliantov, N. et al. (2007). *Collision dynamics of granular particles with adhesion*. Physical Review E 76, 051302.

[13] Morgado, W.A.M.; Oppenheim, I. (1997). *Energy dissipation for quasielastic granular particle collisions*. Physical Review E, Vol. 55, Number 2.

[14] Lin, WH; Daraio, C. (2012). *Experimental Testing of Micro-Particles Collision*. Proceedings of the 2012 Annual Conference on Experimental and Applied Mechanics. Dynamic Behavior of Materials, Volume 1, pp 475-480.

[15] Satoa, K et al. (1999). *Roughening of single-crystal silicon surface etched by KOH water solution*. Sensors and Actuators A 73, 122.

[16] Bauerle, D. *Laser Processing and Chemistry*. Springer 2011.

[17] Lounge, M; Adams, M. (2002). *Anomalous behavior of normal kinematic restitution in the oblique impacts of a hard sphere on an elastoplastic plate*. Physical Review E, VOLUME 65, 021303.